Journal of Environmental Chemical Engineering 14 (2026) 122508

Contents lists available at ScienceDirect

Journal of Environmental Chemical Engineering

journal homepage: www.elsevier.com/locate/jece

Microalgal-based carbon encapsulated iron nanoparticles as novel adsorbents for PFAS removal: From dye proxies to target compounds

Emilio Brivio Sforza [a,b,*], Sara Valsecchi [b], Camilla Mariani [b,c], Silvia Platini [a], Elena Collina [a], Valeria Mezzanotte [a], Marco Mantovani [a]

[a] Università degli Studi Milano-Bicocca, Department of Earth and Environmental Sciences (DISAT), P.zza della Scienza 1, Milano 20126, Italy
[b] IRSA-CNR – Water Research Institute, National Research Council, Via Mulino 19, Brugherio, Monza and Brianza 20861, Italy
[c] Università degli Studi di Milano, Department of Environmental Science and Policy (ESP), via Celoria 26, I-, Milano 20133, Italy

ARTICLE INFO

Keywords:
PFAS
Dyes
Biomass
Iron nanoparticles
Adsorption

ABSTRACT

This study evaluates the performance of microalgal-based carbon-encapsulated iron nanoparticles (ME-nFe) for the adsorption of per- and polyfluoroalkyl substances (PFAS) and synthetic dyes from aqueous solution at laboratory scale. ME-nFe were produced by hydrothermal carbonization (225°C, 3 h) of wastewater-grown microalgae, combining the high reactivity of iron nanoparticles (40% total Fe) with a mixed macro–mesoporous structure supporting them (total pore volume 0.65 $cm^3 \cdot g^{-1}$, BET surface area 117 $m^2 \cdot g^{-1}$). Batch tests at pH 3 and dosages of 1–2 $g \cdot L^{-1}$ showed removal above 90% for medium- and long-chain PFAS (PFUnDA, PFDoDA, PFOS, PFDA, PFNA) and more than 60% removal of PFOA at concentrations typically found in industrial wastewater or landfill leachate (≈15 $\mu g \cdot L^{-1}$) after 200 min, whereas short-chain PFBS, PFHxA and PFPeA were only weakly removed. Dye adsorption at equilibrium (30 min) confirmed strong affinity for cationic dyes at neutral pH and for anionic dyes under acidic conditions. Based on their log Kd, Procion Red, 3B Red, Methyl Orange and Sudan Black closely reproduce the adsorption behaviour of medium- and long-chain PFAS on ME-nFe, supporting their use as cost-effective proxies during adsorbent optimisation. Overall, ME-nFe emerge as a promising adsorbent for PFAS remediation.

1. Introduction

Per and polyfluoroalkyl substances (PFAS) include more than 10.000 synthetic compounds. These molecules are characterized by carbon–fluorine (C–F) bonds that give them highly thermal, chemical, and biological stability. For these reasons they are used in different industrial and consumer applications, from water repellent textiles to fire-fighting foams [1].

They are also crucial in advanced technological sectors such as microelectronics, semiconductors, construction materials, coatings, industrial lubricants, and membranes. Unfortunately, these same properties make PFAS also extremely persistent in the environment and non-biodegradable, leading to bioaccumulation and trophic transfer. Their widespread application led to environmental release during production, use, and disposal of PFAS containing materials, promoting their ubiquitous distribution in water, soil, and biota [2]. Human exposure to PFAS is a major global health concern. Epidemiological and toxicological studies linked high serum concentrations of PFAS to different health problems such as lipid metabolism disorders, high total and LDL cholesterol, hepatic, renal and endocrine dysfunctions. Immunosuppressive effects (i.e. reduced antibody response to vaccines) have also been highlighted in PFAS exposed populations [3]. Chronic exposure, even at low doses, poses cumulative risks due to the long biological half-lives of many PFAS, up to several years for PFOA and PFOS. Their ability to accumulate in the tissues of living organisms leads to biomagnification along food webs [4].

PFAS are characterized by an intrinsic structural complexity due to the different lengths of the carbon chain between molecules, the presence of different functional groups and fluorine atoms. Most PFAS are considered strong acids due to their very low pK_a values, which determine their presence in aqueous environments mainly in anionic form [5]. This influences their interaction with environmental compartments and adsorbent materials. Long-chain compounds bioaccumulate more easily, while short-chain PFAS are usually more soluble in water, more

* Corresponding author at: Università degli Studi Milano-Bicocca, Department of Earth and Environmental Sciences (DISAT), P.zza della Scienza 1, Milano 20126, Italy.
E-mail address: e.briviosforza@campus.unimib.it (E.B. Sforza).

https://doi.org/10.1016/j.jece.2026.122508
Received 10 February 2026; Received in revised form 28 March 2026; Accepted 1 April 2026
Available online 1 April 2026

mobile and difficult to remove. Environmental contamination is further complicated by the presence of ultrashort PFAS [2]. Given these risks, the remediation of PFAS-contaminated environmental matrices is a major technological challenge. Current treatment approaches can be roughly divided between separation and destructive techniques. Separation-based strategies, such as adsorption and filtration, remove PFAS from aqueous media but require subsequent management of the adsorbent materials or concentrated waste stream. Granular activated carbon (GAC) is still the most established technology, effectively removing long-chain PFAS, whereas ion-exchange resins show improved performance for short-chain compounds, even if at higher cost [6]. Nanofiltration and reverse osmosis are also efficient but generate PFAS-rich retentates requiring further treatment.

High-temperature heat treatments, advanced oxidation, electrochemical and plasma-based processes are based on a different approach aimed at completely breaking the C-F bond. The large-scale implementation of these treatments is still limited by high energy requirements and operational complexity. Only high-temperature thermal destruction is actually used on an industrial scale [7–9]. In recent years, research efforts have increasingly focused on the development of advanced adsorbent materials that combine efficiency, selectivity, and environmental sustainability. Among these, biochar-based materials, metal oxides, and functionalized magnetic nanoparticles have shown promising PFAS removal capacities [10]. These materials can be produced through single-step thermochemical processes or with chemical-physical post-treatments of already formed carbonaceous matrices. The presence of doping metals ensures high reactivity and unique chemical-physical properties. Iron in the form of oxides such as magnetite has been exploited to remove PFOA and PFOS from synthetic water on a laboratory scale [11,12]. However, the highly variable efficiencies (17–96%), demonstrate the importance of the starting matrix and synthesis conditions. Zhang et al. worked with an iron-loaded magnetic biochar to remove PFAS from both synthetic water and real matrices, demonstrating, however, the need to further functionalize the material used for adsorption [13]. In fact, the addition of cetyltrimethylammonium bromide (CTAB) to biochar radically increases treatment efficiency (from 15% to 90% for PFOA). However, the modification of an adsorbent through surface functionalization must be assessed from an environmental sustainability perspective. It is important to evaluate the possible toxicity of the reagents used both during the use of the adsorbent and during disposal. Most of the literature highlights a major difficulty in removing short-chain PFAS, whereas medium- and long-chain PFAS are more easily adsorbable due to their greater hydrophobicity [14]. In the environment, there has been a general increase in the concentrations of short-chain PFAS, both due to the replacement of longer molecules that are now regulated (PFOA and PFOS) and the formation of by-products linked to the partial degradation of precursor molecules [15]. This necessitates the development of new adsorbents capable of addressing this issue.

In parallel, biologically based approaches have begun to attract attention, particularly microalgae cultivation systems in the framework of wastewater treatment, which can partially remove recalcitrant contaminants through biosorption and bioaccumulation [16]. Even if biological degradation of PFAS remains extremely limited, the resulting algal biomass can subsequently be valorized as a renewable precursor for the synthesis of functional sorbents [17], including magnetic nanoparticles. In this circular approach, algae serve first as bio-based treatment agents and later as feedstock for advanced PFAS adsorbents, establishing a closed-loop remediation strategy consistent with green chemistry and resource recovery principles [18]. These innovations could be important for more effective and scalable treatment systems, in line with the circular economy concept [19,20]. In this context, magnetic nanoparticles (MNPs) are emerging as promising tools for the removal of PFAS, due to their magnetic separability, high specific surface area and low production cost. Indeed, iron nanoparticles can be rapidly recovered magnetically and modified to enhance PFAS affinity through electrostatic, hydrophobic, and hydrogen-bonding interactions. These adsorbents are versatile and effective toward several targets in environmental remediation. They have been explored for the purification of aqueous matrices from inorganic and organic micropollutants [21], for the in-situ stabilisation of contaminated soils [22], and even for the polishing of gaseous streams [23]. An emerging approach could involve the use of microalgal biomass as a renewable feedstock for magnetic nanoparticle production. Microalgae naturally contain functional groups (i.e. carboxyl, phenolic, and amine) that can improve nanoparticle encapsulation, improving adsorption capacity toward organic and inorganic contaminants and stability. This research focused on the laboratory-scale application of microalgal-based carbon encapsulated iron nanoparticles (ME-nFe) for the removal of PFAS from aqueous solutions. This adsorbent is produced through the hydrothermal carbonization (HTC) process, combining microalgae biomass and an iron salt, using the water content of the carbon matrix as a reaction solvent. Operating at medium-high pressures (25–30 bar), water acts as a catalyst, allowing hydrolysis, condensation and carboxylation reactions to take place, lowering the activation energy. This makes HTC less energy-demanding than more intensive thermochemical processes (pyrolysis and gasification). The analytical complexity and costs associated with the determination and quantification of PFAS (HPLC-MS or UPLC-MS) are an issue that can cause difficulties and delays in the development of effective strategies to adsorb PFAS. Our work suggests the use of substitute compounds that are easier to determine but have characteristics similar to PFAS and therefore show comparable adsorption dynamics (i.e. surface charge and pKa). This approach allows to quickly obtain data on the effectiveness of adsorbent materials in the preliminary study phase. Subsequently, only the most interesting and high-performing prototypes against substitute molecules can be tested on PFAS, validating their actual effectiveness. The use of organic dyes as proxies was also investigated as a practical and low-cost approach to test PFAS adsorption. This topic is gaining attention in the scientific community as certain dyes share physical-chemical features with PFAS, such as the presence of sulfonic groups or the anionic character [24]. To our knowledge, there are no other powder-based adsorbents produced without pyrolytic or high-temperature thermochemical processes, or without post-treatments with hazardous chemical compounds. The novelty of this study lies in proposing a single-step HTC process avoiding high temperatures, to obtain a char-like adsorbent that has the advantages of containing iron nanoparticles. The results obtained both on proxy dyes and PFAS allow to define an operational framework that can reduce time and cost during the engineering phase of novel adsorbents.

2. Materials and methods

2.1. Chemicals

High purity (95–98%) PFAS standards including perfluoropentanoic acid (PFPeA), perfluorohexanoic acid (PFHxA), perfluorooctanoate (PFOA), perfluorononanoate (PFNA), perfluorodecanoate (PFDA), perfluoroundecanoate (PFUnDA), perfluorododecanoate (PFDoDA) perfluorobutanesulfonate (PFBS) and perfluorooctanesulfonate (PFOS) were purchased from Sigma-Aldrich (St. Louis, Missouri, USA). All the standards were solid. Seven organic dyes, i.e. methylene blue (MB), crystal violet (CV), procion red MX-5B (PR), cibacron brilliant red 3B-A (3B Red), sudan black B (SB), malachite green (MG) and methyl orange (MO), were purchased from Sigma-Aldrich. Hydrochloric acid (37%), nitric acid (70%), ammonium hydroxide solution (25%), ammonium acetate (NH_4Ac), formic acid (98%) and HPLC-grade methanol (MeOH) and ethanol (EtOH) were obtained from Merck. Iron (III) nitrate nonahydrate ($Fe(NO_3)_3{\cdot}9\,H_2O$)) (Sigma-Aldrich) was used as the iron source for the production of the ME-nFe. 65% HNO_3, 37% HCl, and 30% H_2O_2 (Sigma-Aldrich) were used for acidic digestion of ME-nFE.

Mass-labelled MPFAC-24ES solution (Wellington Laboratories) was diluted in methanol (1 μg/L) for the preparation of the stable isotope

labelled solution used as internal standard mixture.

2.2. ME-nFe production

Microalgal biomass used as feedstock for hydrothermal carbonization (HTC) was grown at pilot-scale in the high-rate algae–bacteria pond (HRAP) at the Bresso–Niguarda wastewater treatment plant (Milan, Italy). There, microalgae are used as an alternative biological treatment for the liquid phase of anaerobic sludge [25,26]. The biomass, consisting of a mixed community mostly made of *Chlorella* spp. and *Scenedesmus* spp., was harvested by an ELECREM 1 110/230 V centrifugal clarifier. The microalgae paste, obtained by centrifugation, was re-suspended in 200 mL of distilled water to obtain a 30 g TSS·L^{-1} concentration. The suspension was then enriched with 15 g of Fe $(NO_3)_3{\cdot}9\ H_2O$, following a previously published protocol [27]. Finally, the microalgal biomass and iron salt mixture was transferred to a High-Pressure Laboratory Reactor (BR-700, BERGHOF), continuously stirred, and heated to the end temperature of 225°C, and processed with a residence time of 3 h (Fig. 1S of the supplementary material). Hydrothermal conditions are responsible for restructuring microalgal biomass (forming hydrochar) and reducing of the iron nitrate. At this point, both iron oxide nanoparticles and zero-valent iron are formed, doping the microalgal hydrochar that works as carbon support. After overnight cooling, the HTC slurry was vacuum-filtered through a 0.2 μm cellulose acetate membrane. The solid ME-nFe was washed three times with water and ethanol (50:50 v/v) to remove tar and soluble HTC residues, dried at 80°C for 12 h, ground, sieved at 20 μm and stored in a glass vial until use.

2.3. ME-nFe characterization

Nitrogen (N_2) adsorption measurements at 77 K were performed on ME-nFe at the Università degli Studi di Milano using a Coulter SA 3100 analyzer. Specific surface area ($m^2{\cdot}g^{-1}$) was determined by applying the Brunauer–Emmett–Teller (BET) model to the N_2 adsorption isotherm. Pore size distribution was derived from the same physisorption data using the desorption branch. Size and morphology were characterized by SEM (Zeiss Gemini 500 with a field emission gun, FEG), with acceleration voltages of 0.5–30 kV, beam currents of 3 pA-20 nA, and a nominal resolution of 0.6 nm at 15 kV, and by TEM (JEOL JEM-2100Plus, 200 kV) equipped with an 8-megapixel Gatan Rio CMOS camera. TEM samples were prepared by drop-casting onto TEM grids and air-drying. ME-nFe size was also measured based on TEM image elaborations, using the digital image processing program Fiji (ImageJ version 64-bit plugin). Random nanoparticles (n = 318) were chosen and measured from smaller clusters in order to clearly distinguish their boundaries.

Elemental composition was assessed by energy-dispersive X-ray spectroscopy (EDX) on both algal biomass and ME-nFe using the SEM Tescan VEGA TS 5136XM equipped with an energy dispersive microanalysis (EDX) EDAX Genesis 4000. Total iron content was quantified after microwave-assisted acid digestion. 200 mg of ME-nFe was digested with 4 mL of 65% HNO_3, 2 mL of 37% HCl, and 2 mL of 30% H_2O_2 in a microwave digester (Multiwave 5000, Anton Paar). Digestion was carried out at 1000 W for 8 min at 160 °C, followed by 25 min at 1000 W and 200 °C. The samples were then analyzed by inductively coupled plasma–optical emission spectroscopy (ICP-OES; Optima 7000 DV, PerkinElmer). The same analysis was performed to address potential iron leaching from ME-nFe in water. The zero-valent iron content (%Fe^0) was obtained indirectly by exploiting the reaction that develops between metallic iron and hydrochloric acid. This generates hydrogen gas in proportion to the amount of zero-valent iron present in the sample, following the protocol described in another work [23]. Measurement was performed in triplicate, and the system was previously calibrated by determining the hydrogen gas produced by samples of zinc metal powder. The %Fe^0 can be measured based on the stoichiometry of this reaction: $2Fe\ (s) + 6HCl\ (l) \rightarrow 2FeCl\ (s) + 3\ H_2\ (g)$. Crystalline phases were identified by X-ray diffraction (XRD; Bruker D8 Advance, Cu Kα, 40 kV) using a step size of 0.05° 2θ with 3 s per step. FTIR spectroscopy was performed by Perkin Elmer Spotlight 200i instrument. Spectra were recorded in attenuated total reflectance (ATR) mode, applying 32 scans in the 4000–500 cm^{-1} range and a spectral resolution of 2 cm^{-1}. The hydrodynamic size of ME-nFe was evaluated by dynamic light scattering (DLS) tests by a Malvern Zetasizer (Malvern Instruments, Malvern, UK). The point of zero charge (PZC) was determined by the pH-drift method [28]. A 0.01 M NaCl solution was boiled to remove dissolved CO_2, then aliquoted (20 mL) into 50 mL polypropylene tubes. The initial pH (pH_i) was adjusted to predetermined values (from 2 to 10) using 1 M HCl and 0.1 M NaOH. 150 mg of ME-nFe were added to each tube, which was sealed and horizontally shaken for 24 h. After filtration to remove the nanoparticles, the final pH (pH_{24h}) was measured with a pH meter (XS INSTRUMENTS, PC-510). PZC was taken as the value where the difference between the pH_{24h} and pH_i is zero.

2.4. Adsorption experiments with model dyes

Cationic dyes (MB, CV and MG), anionic dyes such as PR, 3B Red and MO, and the neutral hydrophobic dye SB were selected as model compounds as they have different charge classes and molecular properties, including size, aromaticity, functional groups, and hydrophobicity. Preliminary kinetic adsorption experiments were conducted on MB, MG and CV to establish the equilibrium time of adsorption. For each dye, stock solutions were prepared in ultrapure water, previously adjusted to the target pH values of 3, 4, 6, and 7.4. Based on the detection limits of the spectrophotometer, initial dye concentrations were set between 1 and 2.5 mg·L^{-1} . Aliquots of 25 mL from each pH-adjusted solution were transferred into HDPE jars containing pre-weighed ME-nFe nanoparticles to achieve a working dosage of 1 g·L^{-1} . Blank reference samples, (containing ME-nFe and ultrapure water) were also processed at the same time. The suspensions were mixed on an orbital shaker at 200 rpm for 30 min. Temperature was fixed at 25°C as the orbital shaker was put inside a FOC-120E cooled incubator (VELP Scientifica Srl, MB, Italy). Tests were performed in triplicate. At equilibrium, the nanoparticles were magnetically separated using a neodymium magnet at the bottom of each HDPE jar. Under this condition, a larger fraction was attracted within a few seconds, while the finer fraction was collected more slowly. Based on preliminary observation tests, a standardized waiting time of 10 min was adopted for all experiments, which was sufficient to obtain a visibly clear supernatant. The liquid phase was then transferred to a clean vessel by siphoning while maintaining the magnet in position, in order to minimize any carry-over of magnetically retained particles. Samples and controls were both analyzed by UV–Vis spectrophotometry (UV-2600).

2.5. PFAS adsorption experiments

Based on initial hypotheses on the use of dyes as proxies for PFAS removal and on the need to limit the number of samples to be analyzed by UPLC, pH 3 and pH 6 were chosen for the experiment as they gave the best results in removing dyes. First, two separate working solutions at pH 3 and pH 6 were prepared by adding 0.75 mL of the PFAS stock solution (see Table 1S in the Supplementary material) to 500 mL of ultrapure water previously adjusted to the target pH with HCl and NaOH (0.1 M). This procedure yielded nominal concentrations of 15 μg·L^{-1} for PFOS, PFOA, PFNA, PFDA, PFUnDA and PFDoDA, and 7.5 μg·L^{-1} for PFPeA, PFHxA and PFBS. For each condition, 25 mL aliquots of the pH-adjusted PFAS solutions were transferred into HDPE jars containing pre-weighed amounts of ME-nFe, to obtain solid dosages of 1 g·L^{-1} or 2 g·L^{-1} . The dosage of adsorbent was chosen according to previous works with the same nanoparticles on the removal of different micropollutants [18,27]. Suspensions were shaken at 200 rpm and 25°C for 200 min to reach equilibrium. Tests were performed in quadruplicate. At the end of each experiment, the nanoparticles were magnetically recovered (as

previously explained) and the supernatant underwent solid-phase extraction for PFAS analysis. Control samples without adsorbent and procedural blanks (consisting of pH-adjusted ultrapure water without nanoparticles) were also included to assess PFAS losses due to sorption to the vessels or other non-specific removal processes, and/or sample contamination.

2.6. Solid-phase extraction and UPLC analysis

Aqueous samples were extracted according to Method 1633 [29] but using Strata C18-U solid-phase extraction tubes (55 μm, 70 Å, 500 mg/6 mL, Phenomenex, Torrance, CA, USA).

The extracts (both samples test, reference blanks and controls) were analysed using ultra-performance liquid chromatography (UPLC) coupled with high-resolution mass spectrometry (HRMS). The analyses were carried out on a UPLC UltiMate 3000-Vanquish system coupled to an Orbitrap Exploris 120 mass spectrometer (Thermo Fisher Scientific), equipped with an Atlantis Premier BEH C18 AX 5 um, 2.1 × 50 mm (delay column) and Acquity UPLC BEH C18 1.7 um, 2.1 × 50 mm (analytical column). Chromatographic separation was achieved by gradient elution using two mobile phases: (A) 2 mM NH_4Ac with 5% MeOH and (B) 100% MeOH. A "sandwich injection" technique was employed, in which the sample was bracketed between two solvent plugs to minimise band broadening and improve analytical precision. Specifically: 48 μL of 2 mM NH_4Ac + 2 μL IS solution + 2 μL extract + 48 μL 2 mM NH_4Ac. The autosampler was programmed to aspirate and inject this mixture directly into the UPLC system.

The working solutions used at pH 3 and pH 6 were analyzed at time zero and after 200 min of adsorption. Recoveries, calculated with respect to the nominal concentrations (Table 2S), varied between 35–110% for pH 6 and 22–90% for pH 3. (N = 4). Quantification was performed using the isotope dilution method, and the calibration curve (1–200 μg/L; 10 calibration points) was prepared by diluting the PFAS stock solution (Table 1S). The lowest limit of quantitation (LOQ) was set at the lowest calibration level. PFAS concentrations in blanks were always below the LOQ.

2.7. Data analysis

To evaluate the effectiveness of the ME-nFe, removal efficiencies (%) were calculated both for dyes and PFAS as:

$$\text{Removal efficiency} = \frac{C_0 - C_e}{C_0} \times 100 \quad (1)$$

where C_0 and C_e are the initial and equilibrium concentrations respectively, for dyes or PFAS. Sorption affinity was determined by calculating the log Kd values based on experimental data, as log-transformed distribution coefficients provide a direct and unbiased measure of the interaction between each compound and the ME-nFe surface:

$$\text{Log Kd} = \text{Log}\left(\frac{Q_e}{C_e}\right) \quad (2)$$

where Q_e is the amount of contaminants adsorbed by the nanoparticles at equilibrium (μg·g^{-1} or mg·g^{-1} for PFAS and dyes, respectively) and C_e is the equilibrium concentration in the solution at equilibrium (μg·L^{-1} or mg·L^{-1} for PFAS and dyes, respectively).

Statistical analyses were performed to assess the consistency between the adsorption pattern observed for PFAS and for dyes. In cases where the calculated removal was negative, the significance of the change was assessed using a two-tailed paired *t*-test (α = 0.05), testing whether the difference between pre and post treatment concentration was significantly different from zero**.** Pearson correlation was calculated to investigate the relation between PFAS affinities for the ME-nFe and the carbon chain length. The similarity between PFAS and dye removal was quantitatively assessed by calculating the difference between their distribution coefficients:

$$\Delta\text{Log Kd} = \text{Log Kd}_{\text{PFAS}} - \text{Log Kd}_{\text{Dye}} \quad (3)$$

where the distribution coefficients were determined under the same experimental condition of 1 g·L^{-1} of adsorbent, ensuring data consistency across both pH 3 and pH 6 tests. A $\Delta\text{Log Kd} \leq 0.1$ was chosen as a high similarity threshold for comparable adsorption. This relationship was graphically visualized through a Principal Component Analysis (PCA) using the combined dataset from both pH 3 and pH 6 experiments. The PCA was built using two principal components: pH and Log Kd, which together explained the total variance. The two variables had been standardized in order to obtain a comparable scale following the formula:

$$Z_{ij} = \frac{(X_{ij}) - \bar{x}_j)}{S_j} \quad (4)$$

where X_{ij} is the original datum for the j variable; $\bar{x}_j$ is the average of the j variable, and s_j is the standard deviation of the j variable.

3. Results and discussion

3.1. Characterization of microalgal-based carbon encapsulated iron nanoparticles

ME-nFe appears as globular particles with a cauliflower-like texture (Fig. 1). At the 200 nm scale, compact sub-micrometric agglomerates are evident, composed of rough primary particles in the nanometric range. Low-magnification TEM images (Fig. 2) show clusters of nano-sized particles (≃10–50 nm) with strong mass–thickness contrast. The magnified view (50 nm scale bar, green rectangle) displays clear lattice fringes, confirming the crystalline nature of the iron-oxide domains embedded within larger aggregates. Inside the clusters, individual nanoparticles had an average diameter of 9.4 ± 3 nm (n = 318). Size distribution can be seen in Fig. 2S of supplementary material. Additionally, DLS (intensity-weighted) showed a highly polydisperse, multimodal distribution with a dominant population around ~230 nm and additional aggregates at ~430 nm and in the micron range (~4 μm) (Fig. 3S of the supplementary material). The high PdI (~0.91) indicates strong aggregation/heterogeneity. A similar property has been observed in other adsorbents, such as biochar-doped nZVI produced from spent coffee grounds [30]. The authors report hydrodynamic size values ranging from ~514–2112 nm and explicitly discuss that, in polydisperse/agglomerated systems, DLS can be dominated by a few large clusters and overestimate the hydrodynamic size [31].

The ME-nFe showed a BET specific surface area of 117 m^2·g^{-1}, higher than char-materials obtained by hydrothermal carbonization (HTC) without post-activation [32] but lower than that of iron-loaded microalgae after high-temperature pyrolysis at 750 °C (201 m^2·g^{-1}) [33]. This difference was expected: pyrolysis conditions are harsher and etch the carbon framework more deeply, generating additional microporosity and thus higher BET area. In practice, there is a trade-off as production temperature increases, porosity and material stability tend to rise, while yield decreases and both production costs and environmental impacts increase. Hence, HTC-derived materials typically have lower BET surface area, but they can offer advantages in scalability and ecological footprint [34]. The N_2 adsorption–desorption isotherm (Fig. 3A) exhibits a small hysteresis loop consistent with an IUPAC Type IV–H3 profile (≈0.4–0.9 p/p$_o$), indicative of a mesoporous material with significant interparticle and macroporous voids. Fig. 3B, C provide more insight on the porosity of ME-nFe. The total pore volume was 0.66 cm^3 ·g^{-1} obtained from the adsorption branch at p/p$_o$ ≃ 0.99. This datum is higher than the one reported by Kozyatnyk et al., in biochar (without iron) produced from algal biomass under the same temperature and residence time conditions (0.13 cm^3·g^{-1}), but similar to that obtained by Calderon et al. (0.59 cm^3·g^{-1}) on carbon-encapsulated iron

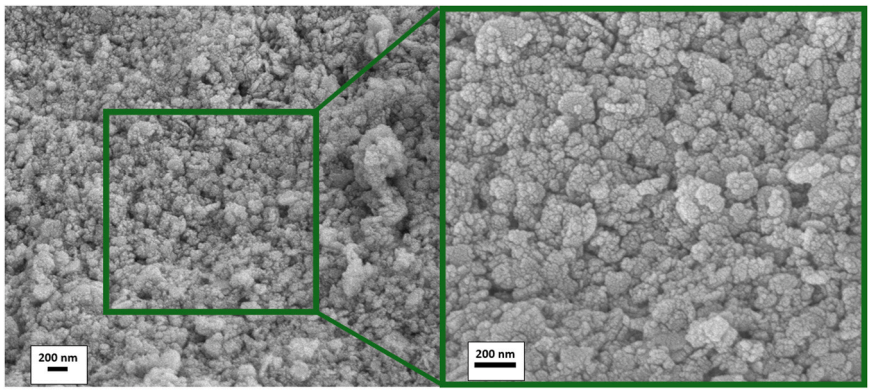

Fig. 1. SEM images of ME-nFe showing aggregates with globular morphology. The green area is magnified on the right to better appreciate the details of the cauliflower-like structures.

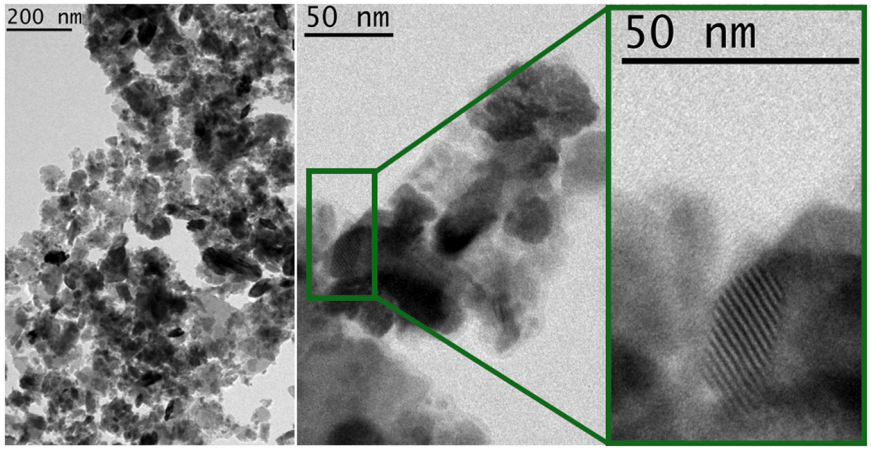

Fig. 2. TEM images of the of ME-nFe. The low-magnification image on the left shows an aggregated morphology with irregular particle clusters. The intermediate magnification (centre) highlights the granular structure where lattice fringes are visible. On the right this area is further magnified (green rectangle) to reveal the lattice fringes showing crystalline domains.

nanoparticles (CE-nFe) obtained through HTC of olive mill waste [32, 35]. Considering the similarity between ME-nFe and CE-nFe, the presence of iron during the HTC process might help to deconstruct the carbon matrix, developing greater porosity.

The pore size distributions derived by the Barrett–Joyner–Halenda (BJH) method from the desorption branch showed heterogeneity, 42% was made of macropores (>80 nm), 38% of mesopores (20–80 nm), and the remaining ≃10% of sub-6 nm pores (micropores + very small mesopores). This meso-macroporous structure is advantageous for mass transport, enabling faster intraparticle diffusion and rapid access to reactive sites. In practical terms, compared with predominantly microporous sorbents (e.g., many activated carbons), such a distribution can reduce adsorption contact times, an asset for tertiary wastewater treatment where hydraulic residence time is limited. Given the known limitations of BJH analysis for accurately resolving micropores and very small mesopores, the sub-10 nm region should be regarded as only indicative.

Microwave-assisted acid digestion followed by ICP-OES quantified a total Fe content of 39.5 wt% in ME-nFe. The zero-valent iron content (% Fe^0) was 9 ± 1 wt%. Both data are similar to the ones reported by Calderon et al. (42.5% and 10.6%). The X-ray diffraction (XRD) of the ME-nFe sample confirmed a crystalline iron-oxide phase consistent with hematite (α-Fe_2O_3; PDF 01–084–0311) and with quartz (α-SiO_2; PDF 01–070–2540). As shown in Figs. 4S and 5S of the supplementary material, the characteristic hematite reflections match both in position and relative intensity, while the strong quartz peak around ≃26.6° confirms silica, which could be explained by the presence of diatoms in the microalgal biomass used to produce ME-nFe. A broad diffuse hump in the range 15–35° indicates an amorphous background attributable to the carbonaceous matrix produced by HTC. The amorphous phase is the most abundant (72% wt), while hematite and quartz account for 21.5% and 6.5% wt, respectively. Quantitative analysis was performed using the Rietveld method.

Fig. 6S-B of the supplementary material confirms the presence of iron, oxygen and carbon. The nanoparticles were also composed of less abundant elements such as aluminium, phosphorus and calcium. The same elements, except for iron, can also be detected in the microalgal biomass EDX spectrum, used for the HTC process (Fig. 6S-A). Similar elements were detected by Binda et al. in microalgae-derived biochars [36]. The ATR-FTIR spectrum of ME-nFe (Figure 7S of supplementary material) showed characteristics associated with a carbonaceous material containing Fe, including a broad O–H stretching band at ~3400 cm^{-1} , weak aliphatic C –H vibrations at ~2920–2850 cm^{-1} , a band near 1600 cm^{-1} related to surface oxygenated groups and adsorbed water, and low wavenumber absorptions consistent with Fe–O vibrations. The presence of iron oxides was confirmed by Passalacqua et al. on nanoparticles produced with the same protocol and biomass. XPS data revealed a carbon-rich surface functionalized with oxygen together with iron species. In the C 1 s spectrum, signals were detected at ~286 and ~288–289 eV, attributable to oxygenated functional groups (hydroxyl/ether, carbonyl, and carboxyl groups). In the Fe $2p_{3/2}$ region, contributions at 708.2 and 711.4 eV were detected, indicating the presence

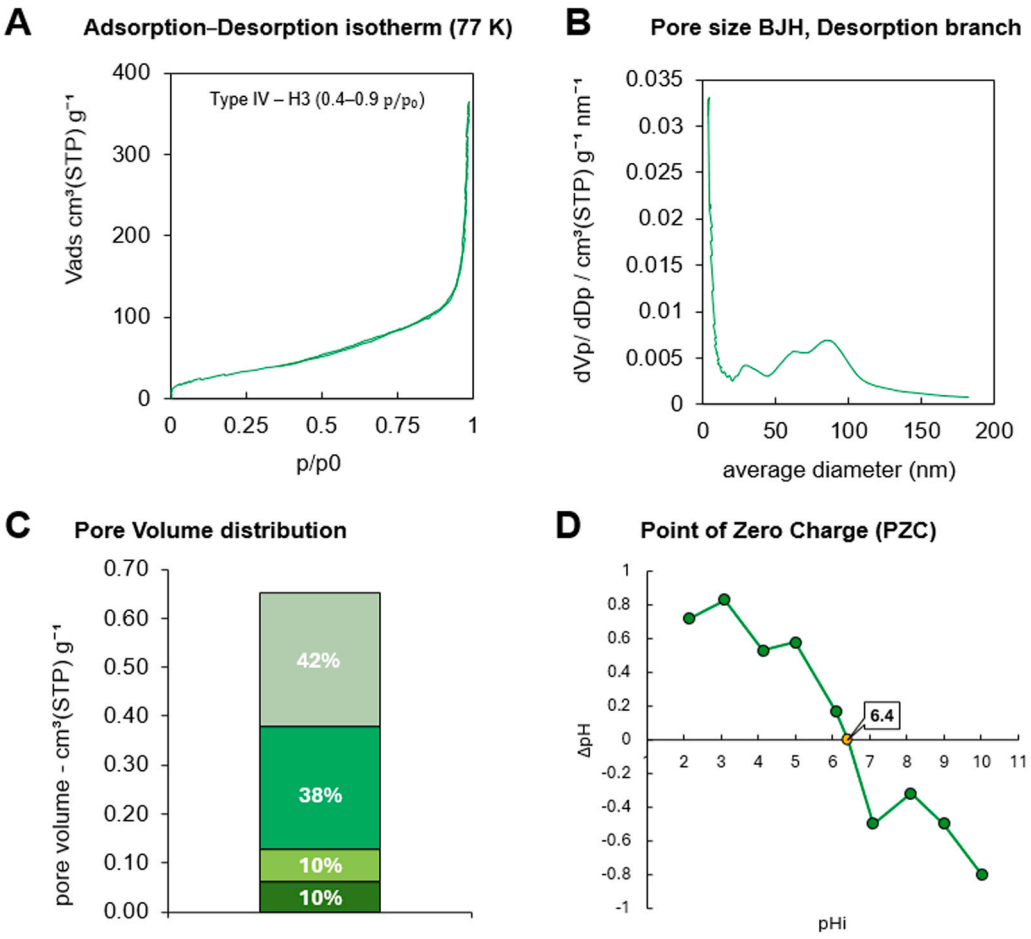

Fig. 3. Nitrogen adsorption-desorption isotherm of ME-nFe (A); pore size distribution of ME-nFe (B, C); Point of Zero Charge (PZC) graph for ME-nFe (D).

of reduced Fe and Fe (III) species [23]. This would suggest that the iron species were immobilized/anchored in the microalgal matrix of ME-nFe. ICP analysis on water eluates at pH 3 and 6 demonstrated that the HTC process was effective in shielding the iron, preventing fast aging and release in water even after 48 h (Table 3S of supplementary material). The PZC was 6.4 (Fig. 3D). This value is consistent with similar iron doped adsorbent [37]. The PZC is a key parameter governing adsorption in aqueous solution. It is the pH at which ME-nFe has a net neutral surface charge; at pH values above that threshold, the surface is predominantly negatively charged, while below it is predominantly positively charged.

3.2. Adsorption experiments with model dyes

Across all tested dyes, adsorption equilibrium was consistently achieved within 30 min, indicating rapid surface interactions between sorbate molecules and the nanoparticle surface (Figures 8S). In fact, the difference in adsorption efficiency between 30 and 200 min was not statistically significant (p-value>0.05). This equilibrium time was selected for the pH-dependent batch experiments. The removal of cationic dyes (MB, MG and CV) was more efficient under neutral/slightly alkaline pH, reaching 90–100%, and dropped to 20–40% at pH 3. On the other hand, anionic dyes (PR, 3B Red and MO) displayed an opposite trend with maximum removal at pH 3 (70–95%). The greater variability in terms of the molecular properties of anionic dyes (compared to cationic dyes) could explain the differences in the ME-nFe efficiency. In fact, additional mechanisms, other than mere surface charge, could be involved. This could explain what was observed for SB. This neutral and hydrophobic dye followed the trend of PR, 3B Red and MO, but with a significantly higher removal rate (≃84–87%) at pH 3–4 probably due to hydrophobic and π–π interactions between the aromatic rings of the dye and the carbonaceous matrix of ME-nFe; at pH 7.4 the removal efficiency dropped to about 10%. The lowest results obtained in the removal of anionic dyes have already been observed with biochar produced from the pyrolysis of switchgrass. However, the authors hypothesize that π-π interactions may mitigate electrostatic repulsions at unfavorable pH conditions [38]. Fig. 4 summarizes the pH-dependent adsorption of model dyes on ME-nFe and highlights the role of surface charge.

3.3. PFAS adsorption experiments

For comparative purposes PFAS adsorption was conservatively assessed at 200 min. Indeed, this choice is consistent with the range of equilibrium contact times reported for PFAS sorption on other adsorbents [39,40]. As shown in Fig. 5, the best result for PFAS removal was achieved at pH 3. At the dosage of 2 $g \cdot L^{-1}$, removals reached 99.7 ± 0.1% for PFUnDA and PFDoDA, 97 ± 2% for PFDA, and 96 ± 2% for PFOS, while intermediate removals were recorded for PFNA (88 ± 4%) and PFOA (62 ± 7%). Short-chain compounds such as PFBS, PFHxA and PFPeA were not effectively removed (26 ± 26%, 18 ± 32% and 16 ± 33%, respectively), and this was consistent with their higher solubility and weaker hydrophobic interactions. Although the highest efficiency was obtained at 2 $g \cdot L^{-1}$, the results at 1 $g \cdot L^{-1}$ were already remarkable, with removals exceeding 90% for PFOS and PFDA, and being nearly complete for the long-chain PFUnDA and PFDoDA. The increase in dosage mainly enhanced adsorption for a few specific compounds (PFOA, PFNA, PFDA and PFOS), with removal improving on

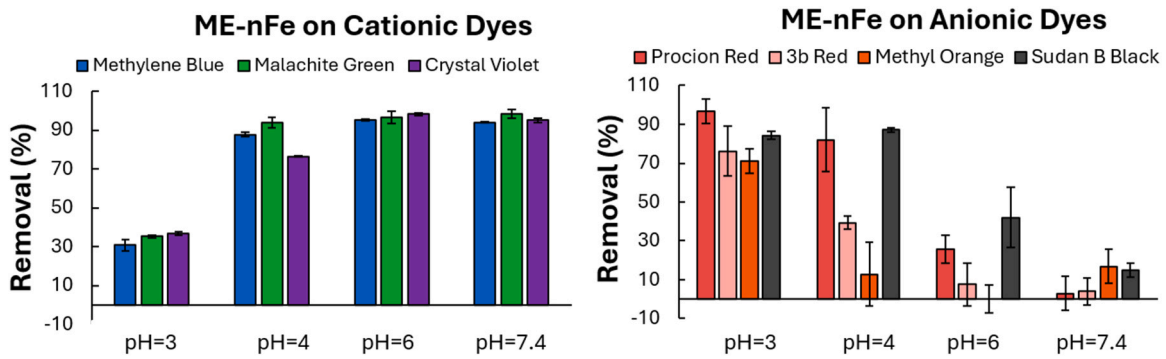

Fig. 4. Adsorption performance of ME-nFe for cationic, anionic and hydrophobic dyes (C_o = 1 mg·L^{-1} for PR, 3B Red, CV, MG and MO and 2.5 mg·L^{-1} for MB and SB; ME-nFe = 1 g·L^{-1}; eq_{time} = 30 min; T = 25 °C). Data are presented as average and standard deviations (n = 3).

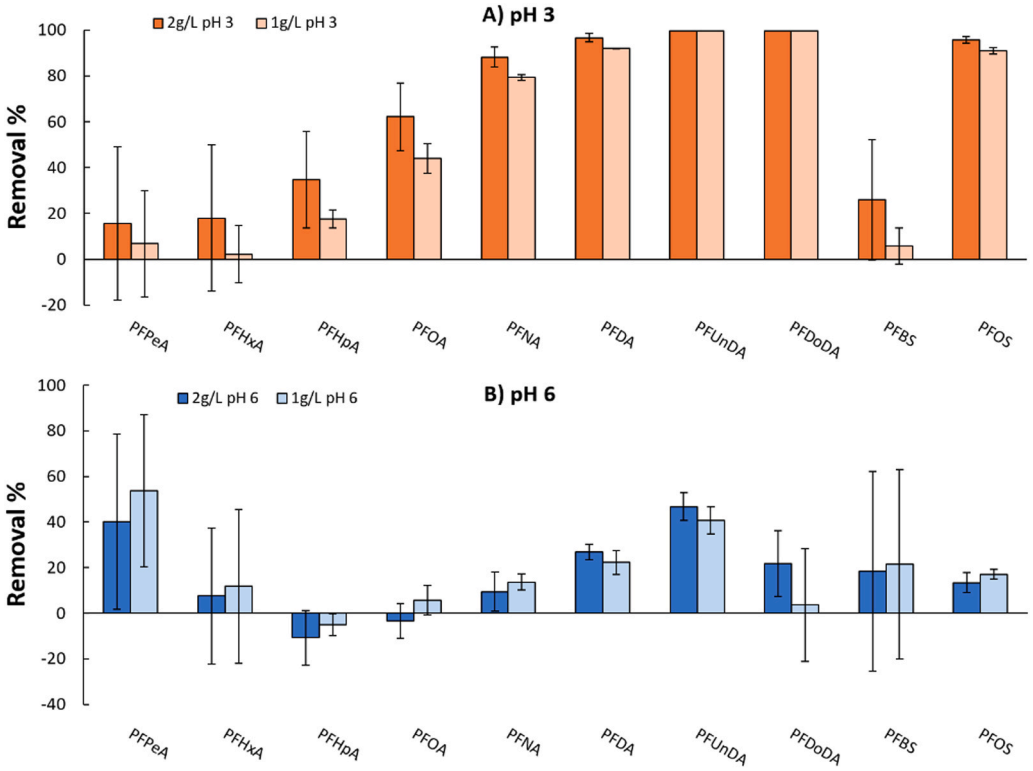

Fig. 5. Percent removal of Perfluoropropanoic acid (PFPeA), Perfluorohexanoic acid (PFHxA), Perfluoroheptanoic acid (PFHpA), Perfluorooctanoic acid (PFOA), Perfluorononanoic acid (PFNA), Perfluorodecanoic acid (PFDA), Perfluoroundecanoic acid (PFuNDA), Perfluorododecanoic acid (PFDoDA), Perfluorobutanesulfonic acid (PFBS) and Perfluorooctanesulfonic acid (PFOS). Figure A) shows results at pH 3 for both ME-nFe dosages; Figure B) shows results at pH 6. Data are presented as average and standard deviations (n = 4). In cases where removal was negative, the difference between initial (t_0) and final concentrations after treatment was not statistically significant ($p > 0.05$).

average by 18–20%. Overall, these results indicate that at pH 3 the ME-nFe nanoparticles exhibit sufficient adsorption capacity already at 1 g·L^{-1} for long- and medium-chain PFAS, while a further increase in dosage primarily benefits compounds with weaker electrostatic or hydrophobic interactions. At pH 6, however, adsorption performance dropped dramatically: PFOS removal ranged between 13–17%, PFOA removal became negligible (−3–6%), and even long-chain PFAS showed efficiencies below 30–40%. In general, short-chain PFAS exhibited broader standard deviations at both pH 3 and pH 6, indicating lower affinity for the ME-nFe surface. These species might be more sensitive to variations in surface charge distribution and to the presence of competing anionic species. Among them, PFPeA was slightly better removed at pH 6, though with considerable variability, confirming its weaker and less predictable interaction with the adsorbent compared to longer-chain PFAS. At pH 3, PFAS adsorption increased with increasing carbon chain length (Pearson r = 0.91, $p < 0.05$), in accordance with what is reported in the literature, where longer-chain PFAS generally show greater sorptive affinity due to greater hydrophobicity [24]. This trend was expected (Fig. 6), since short-chain PFAS are generally more soluble in water. Overall, the data support a dual contribution: (i) electrostatic attraction between the anionic terminal groups of PFAS and protonated surface sites under acidic conditions (pH < PZC) and (ii) hydrophobic contributions associated with the perfluoroalkyl tail, as indicated by the dependence of Log Kd on chain length. Near the PZC (pH 6), the reduction in net surface charge attenuates the electrostatic driving force, resulting in lower Kd values and less selectivity with respect to chain length. Furthermore, when dealing with mixtures (even in distilled water), competition for the active sites of the nanoparticles

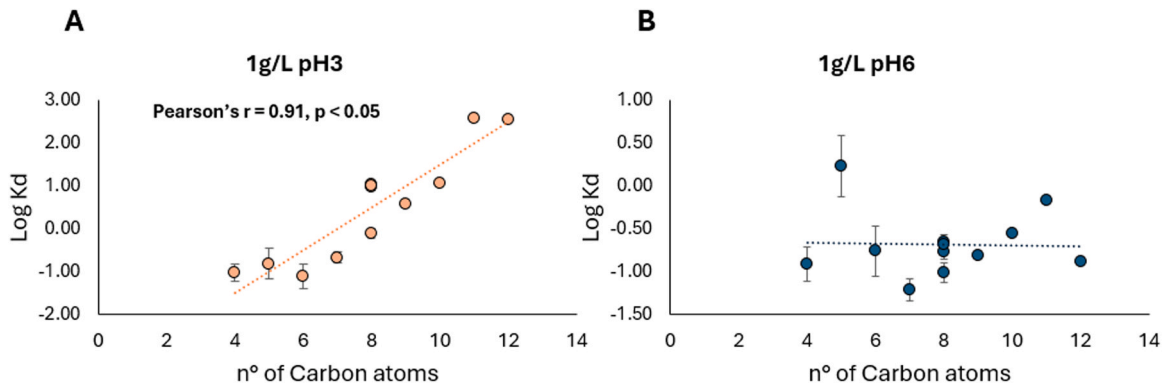

Fig. 6. PFAS affinity for ME-nFe (as experimental Log Kd) as a function of the number of carbon atoms. Data are expressed as average and standard deviation (n = 4). While a strong and positive correlation can be observed for pH 3, no correlation can be noted for pH 6 where electrostatic interactions are not favourable. However, even if the Log Kd values are smaller, a positive trend can be noted for C7–C11 PFAS even at pH 6.

might hinder the effectiveness toward shorter compounds [14]. The FTIR spectra of ME-nFe before and after PFAS adsorption were largely superimposable, with no significant shifts in peaks or appearance of new diagnostic bands (Figure 7S of supplementary material). This suggests that PFAS adsorption did not induce detectable changes in the overall spectral profile of the adsorbent under the tested conditions, probably due to the low adsorbed mass and/or overlap with the intrinsic bands of the material. The shift in performance at different pH can be explained by the PZC (6.4) of the ME-nFe nanoparticles, consistent with what was previously observed with anionic dyes. As PFAS are deprotonated at all the tested pH, electrostatic interactions between PFAS and nanoparticles are better promoted at pH 3 when ME-nFe are positively charged. The sharp decline in adsorption at pH 6 therefore reflects the loss of favourable electrostatic interactions.

Literature studies on similar adsorbents support the role of surface charge and functionalization in PFAS adsorption. For example, biochar produced through pyrolysis and enriched with iron, but characterized by relatively high PZC values, showed efficient removal of PFOA and PFOS at near-neutral pH, in some cases exceeding 96% [11], while materials with PZC values closer to that of ME-nFe generally showed more moderate removals under similar conditions (e.g., 18–36%) [12,41]. Similarly, further cationic functionalization markedly improved performance, as CTAB-modified magnetic biochar increased PFOA removal from approximately 15% to 90–95% [13], confirming the importance of favorable electrostatic interactions. In contrast, the more pronounced pH dependence observed for ME-nFe, with much higher removals under acidic conditions than at pH 6, is consistent with their lower PZC. Differences in BET specific surface area, pore structure, and the simultaneous presence of multiple PFAS in the present study may also have contributed to the lower efficiencies observed under less favorable pH conditions.

Altogether, the literature clearly indicates that the PZC is the major factor controlling PFAS adsorption, often outweighing the effect of specific surface area alone. The PZC depends strongly on the feedstock composition, synthesis temperature, and the type of functionalization applied to the adsorbent. These factors control the mineral phases, the density of surface hydroxyl groups, and the degree of iron oxidation. As a result, comparisons across studies must be made cautiously, as materials with different precursors or preparation routes often show divergent PFAS removal behaviour even under similar experimental conditions. Moreover, most literature data still rest on adsorption tests made at unrealistic PFAS concentrations (on the order of $mg \cdot L^{-1}$ to $g \cdot L^{-1}$). Indeed, one of the major difficulties in water treatment is to deal with trace pollutants. Adsorbents with high PZC values remain positively charged over a wider pH range, achieving efficient removal even in near-neutral or slightly alkaline waters. In contrast, materials with lower or moderately acidic PZC, such as ME-nFe (6.4), perform optimally at low pH where the surface is strongly protonated. Under these conditions, adsorption proceeds through combined electrostatic attraction, hydrogen bonding, and ligand exchange mechanisms between surface hydroxyls and the functional headgroups of PFAS molecules.

In this work, the similarity between PFAS and dye removal was quantitatively assessed by comparing their distribution coefficients through the relation: $\Delta\text{Log Kd} = \text{Log Kd}_{\text{PFAS}} - \text{Log Kd}_{\text{dye}}$. These comparisons were performed under the same experimental condition of 1 $g \cdot L^{-1}$ of adsorbent, ensuring data consistency and comparability across both pH 3 and pH 6 tests. As shown in Table 1, at pH 3, ΔLog Kd values were close to zero comparing PR, 3B Red, and SB with medium and long-chain PFAS (PFNA, PFDA, PFUnDA, PFDoDA). This demonstrates a strong correspondence between the two classes of compounds, suggesting that these dyes can be considered valid analytical proxies under acidic conditions. Generally, ΔLog Kd values were higher than 0.3 when considering cationic dyes such as MB, CV, and MG with medium and long-chain PFAS. This proved that those PFAS were generally adsorbed more efficiently than cationic dyes. The only exceptions were the associations between CV and PFNA (ΔLog Kd =0.26), and between MB and MG with PFOA (ΔLog Kd =0.26 and 0.18, respectively). On the other hand, short-chain PFAS were less adsorbed than dyes at this pH.

At pH 6 (Table 1), overall adsorption efficiency decreased markedly for both PFAS and anionic dyes, but several interesting correlations persisted. MO, 3B Red, and PR displayed affinity ($\Delta\text{Log Kd} \approx 0.01 - 0.3$) with most PFAS, including PFHxA, PFHpA, PFOA, PFNA, PFDA, PFUnDA, PFDoDA, and PFBS. This suggests that, even though adsorption was less efficient under near-neutral conditions, these dyes continued to behave in a comparable manner to PFAS, making them suitable for qualitative correlation studies. On the other hand, cationic dyes (MB, CV and MG) were always fully removed, giving negative ΔLog Kd values for most comparison, indicating a better adsorption of such compounds than that of PFAS.

Sörengård et al. also investigated the correlation between PFAS and dye adsorption across 39 novel adsorbents through seven-day batch experiments. The tests were performed using 2.5 $g \cdot L^{-1}$ of each adsorbent at pH 7.5, with an initial PFAS concentration of 100 $\mu g \cdot L^{-1}$ and variable dye concentrations ($mg \cdot L^{-1}$), under agitation at 100 rpm. The removal of CV was found to correlate positively with PFBA and PFNA, whereas MB removal showed significant correlation with PFBA, PFPeA, and PFHxA. Despite the different anionic dyes evaluated, the conclusion that CV can be used as a proxy for PFNA removal is partially consistent with the behaviour observed for ME-nFe in the present study.

4. Limitations and future perspectives

In this study, ME-nFe was evaluated under controlled conditions

Table 1
ΔLog Kd = Log Kd_{PFAS} − Log Kd_{dye} supporting the similarity between PFAS and dyes for ME-nFe.

pH 3

Δ Log Kd Table	PFPeA	PFHxA	PFHpA	PFOA	PFNA	PFDA	PFUnDA	PFDoDA	PFBS	PFOS
Methyl orange	-1.21	-1.50	-1.07	-0.50	0.19	0.66	2.18	2.15	-1.41	0.62
Methylene blue	-0.45	-0.74	-0.32	0.26	0.95	1.42	2.94	2.91	-0.65	1.38
Malachite Green	-0.53	-0.82	-0.39	0.18	0.87	1.34	2.86	2.83	-0.73	1.30
Procion Red	-1.88	-2.17	-1.74	-1.17	-0.48	-0.01	1.51	1.48	-2.08	-0.05
Crystal Violet	-1.14	-1.43	-1.00	-0.43	0.26	0.73	2.25	2.22	-1.34	0.69
3B Red	-1.41	-1.71	-1.28	-0.70	-0.01	0.46	1.98	1.95	-1.62	0.41
Sudan Black B	-1.34	-1.63	-1.20	-0.63	0.06	0.53	2.05	2.02	-1.54	0.49

pH 6

Δ Log Kd Table	PFPeA	PFHxA	PFHpA	PFOA	PFNA	PFDA	PFUnDA	PFDoDA	PFBS	PFOS
Methyl orange	1.09	0.09	-0.36	-0.16	0.04	0.30	0.69	-0.03	-0.07	0.20
Methylene blue	-0.88	-1.88	-2.33	-2.13	-1.93	-1.67	-1.28	-2.00	-2.03	-1.77
Malachite Green	-0.93	-1.93	-2.38	-2.18	-1.98	-1.72	-1.33	-2.05	-2.09	-1.82
Procion Red	0.64	-0.36	-0.81	-0.61	-0.41	-0.15	0.24	-0.48	-0.51	-0.25
Crystal Violet	-0.62	-1.62	-2.07	-1.88	-1.67	-1.41	-1.03	-1.74	-1.78	-1.51
3B Red	0.99	-0.01	-0.47	-0.27	-0.07	0.19	0.58	-0.14	-0.17	0.10
Sudan Black B	0.44	-0.56	-1.02	-0.82	-0.62	-0.36	0.03	-0.69	-0.72	-0.45

No similarity	Δ Log Kd < –0.3 The dye was removed more than the PFAS
High similarity	Δ Log Kd≤ **0.1** Dye and PFAS have the same affinity for ME-nFe.
Moderate similarity	**0.1 ≤ Δ Log Kd ≤ 0.2 Dye and PFAS have similar affinity for ME-nFe.**
Low similarity	0.2 ≤ Δ Log Kd ≤ 0.3 Dye and PFAS **have low affinity** for ME-nFe.
No similarity	Δ Log Kd > 0.3 The PFAS was removed more than the dye

(distilled water) and showed a marked dependence on pH: maximum efficiency was observed in an acidic environment (pH 3), consistent with a mechanism in which the electrostatic contribution becomes dominant below the PZC (6.4). This operating window constitutes a significant limit for real application; therefore, the design of variants of the adsorbent with a PZC shifted towards higher values is a priority, to maintain attraction towards anionic PFAS even at pH close to neutral. This could be achieved by (i) introducing oxide/hydroxide phases with positive functional groups (e.g. Al/Mg/Zn) during the impregnation of the pre-HTC biomass or by post-deposition, and/or (ii) functionalization with cationic groups (e.g. amine/polymer coatings) capable of increasing the effective positive charge of the material.

Regeneration of ME-nFe after PFAS adsorption was not directly addressed in this work and requires dedicated studies. Thermal and chemical strategies are common methods for the regeneration of spent adsorbents. Thermal treatment requires high temperatures for PFAS degradation that can lead to unwanted structural changes in the adsorbent. Spent ME-nFe, rich in oxides and oxygenated functionalities, could be treated by pyrolysis under inert conditions so long as the hematite and metallic iron phases are not lost by oxidation. Recently, hydrothermal carbonization has also been studied as a method for degrading PFAS on spent carbons, but it appears to be more effective for degrading PFCAs than sulfonated PFAS [42]. A “capture-and-destroy” approach could be evaluated, exploiting the iron in the spent ME-nFe as catalyst for photo-radical processes (e.g. photo-Fenton). This would promote the degradation/defluorination of PFAS concentrated on the surface of ME-nFe. In this case, the integrity of the material after treatment should be guaranteed, in addition to accurate detection of all possible degradation products of the original PFAS compounds. Chemical treatments consist of desorption processes that must counteract

hydrophilic and hydrophobic interactions. Figure 9S of the supplementary material shows a preliminary study on the consecutive use of ME-nFe for multiple cycles to remove methylene blue from distilled water. The adsorption capacity of the nanoparticles decreases with the number of adsorption cycles (88, 84, 75, 64, 52 and 42%), consistent with the decrease in available active sites. However, chemical regeneration using methanol or ethanol (as an alternative, as shown in Figure 9S of the supplementary material) allows the dye to be desorbed, restoring the original adsorption capacity for four consecutive cycles. Consecutive use and chemical regeneration would suggest that ME-nFe are stable under the tested conditions. Although this experiment was only carried out on methylene blue, it seems promising also for PFAS. Regeneration capacities (>94%) through chemical washing in methanol and ethanol were reported both for long and short-chain PFAS (PFOA, PFOS and GenX) [43,44].

Background ions and organic matter might reduce the effectiveness of PFAS adsorption on ME-nFe in complex environmental aqueous matrices. Competition, electrostatic shielding and fouling have not yet been quantified. Preliminary information on this subject has been obtained by studying the adsorption of Procion red (PR) in different samples: ultrapure water, low-mineral bottled water (San Benedetto), municipal effluent collected before UV disinfection and centrifuged digestate (liquid fraction of anaerobic sludge). Adsorption tests were carried out evaluating a starting dye concentration of 2.5 $mg \cdot L^{-1}$ under the same conditions explained in the previous section involving dyes (pH 3, 1 $g \cdot L^{-1}$ ME-nFe, 30 min, 25°C). The data, included in the supplementary material (Figure 10S), show that PR was still effectively removed in all four matrices (80–97%), although a progressive decrease in treatment efficiency was observed with increasing matrix complexity, with the lowest removal found in digestate. This trend is consistent with the expected matrix effect: inorganic species and dissolved/colloidal organic matter may progressively reduce the availability of adsorption sites. These observations are also similar to our previous study on ME-nFe for the removal of pharmaceutical compounds and antibiotics [27], where no appreciable decrease in removal was observed when switching from distilled water to effluent, while a marked loss of performance occurred in the liquid fraction of anaerobic sludge. Although these observations must also be verified for PFAS removal, the behavior of ME-nFe in the effluent is promising.

5. Conclusions

This study suggests that carbon-encapsulated iron nanoparticles based on microalgae (ME-nFe) produced by hydrothermal carbonization can help address two urgent environmental problems simultaneously: the valorisation of biomass cultivated in wastewater and the removal of persistent contaminants such as PFAS. ME-nFe was been tested on a laboratory scale to remove a mixture of PFAS from synthetic aqueous solutions. Adsorption tests on PFAS reveal that ME-nFe are particularly effective at pH 3 for medium- and long-chain PFAS (PFUnDA, PFDoDA, PFOS, PFDA, PFNA) with removal efficiencies exceeding 90% and reaching over 60% removal for PFOA. At this pH, the nanoparticles proved effective even at the lowest dosage tested (1 $g\ L^{-1}$). ME-nFe have also been tested for the removal of dyes from aqueous solutions to identify which of them may have adsorption dynamics comparable to certain PFAS. By comparing the experimental affinity values for ME-nFe (Log Kd), the anionic dyes Procion Red, 3B Red, and Sudan Black B appeared to be the best proxies for the removal of medium- to long-chain PFAS (PFNA, PFDA and PFOS). Electrostatic forces (specifically favoured at acidic pH) and hydrophobic interactions both contribute to the adsorption of dyes and PFAS on ME-nFe.

The results obtained are promising but highlight a major limitation in the use of this adsorbent at environmental pH. By modifying the synthesis process to overcome this limitation, ME-nFe could be effective against PFAS at concentrations typically found in industrial wastewater or landfill leachate. Using the dyes identified as proxies could help evaluate different adsorbent prototypes with fast screening tests, prior to proving them on PFAS with costly HPLC analysis.

CRediT authorship contribution statement

Valeria Mezzanotte: Writing – review & editing, Supervision, Conceptualization. **Elena Collina:** Writing – review & editing. **Silvia Platini:** Formal analysis. **Marco Mantovani:** Writing – original draft, Investigation, Formal analysis, Data curation, Conceptualization. **Camilla Mariani:** Formal analysis. **Sara Valsecchi:** Writing – review & editing, Supervision, Formal analysis. **Emilio Brivio Sforza:** Writing – original draft, Investigation, Formal analysis, Data curation, Conceptualization.

Declaration of Generative AI and AI-assisted technologies in the writing process

During the preparation of this work the authors used ChatGPT for writing and revising the manuscript. After using this tool/service, the authors reviewed and edited the content as needed and take full responsibility for the content of the published article.

Declaration of Competing Interest

The authors declare that they have no known competing financial interests or personal relationships that could have appeared to influence the work reported in this paper.

Appendix A. Supporting information

Supplementary data associated with this article can be found in the online version at doi:10.1016/j.jece.2026.122508.

Data availability

Data will be made available on request.

References

[1] J. Glüge, M. Scheringer, I.T. Cousins, J.C. Dewitt, G. Goldenman, D. Herzke, R. Lohmann, C.A. Ng, X. Trier, Z. Wang, An overview of the uses of per- And polyfluoroalkyl substances (PFAS), Environ. Sci. Process. Impacts 22 (2020) 2345–2373, https://doi.org/10.1039/d0em00291g.
[2] L.G.T. Gaines, Historical and current usage of per- and polyfluoroalkyl substances (PFAS): a literature review, Am. J. Ind. Med. 66 (2023) 353–378, https://doi.org/10.1002/ajim.23362.
[3] S.E. Fenton, A. Ducatman, A. Boobis, J.C. DeWitt, C. Lau, C. Ng, J.S. Smith, S. M. Roberts, Per- and polyfluoroalkyl substance toxicity and human health review: current state of knowledge and strategies for informing future research, Environ. Toxicol. Chem. 40 (2021) 606–630, https://doi.org/10.1002/etc.4890.
[4] G.M. Sinclair, S.M. Long, O.A.H. Jones, What are the effects of PFAS exposure at environmentally relevant concentrations? Chemosphere 258 (2020) https://doi.org/10.1016/j.chemosphere.2020.127340.
[5] K.U. Goss, The pKa values of PFOA and other highly fluorinated carboxylic acids, Environ. Sci. Technol. 42 (2008) 456–458, https://doi.org/10.1021/es702192c.
[6] T.D. Appleman, C.P. Higgins, O. Quiñones, B.J. Vanderford, C. Kolstad, J. C. Zeigler-Holady, E.R.V. Dickenson, Treatment of poly- and perfluoroalkyl substances in U.S. full-scale water treatment systems, Water Res 51 (2014) 246–255, https://doi.org/10.1016/j.watres.2013.10.067.
[7] J.N. Meegoda, B. Bezerra de Souza, M.M. Casarini, J.A. Kewalramani, A review of PFAS destruction technologies, Int. J. Environ. Res. Public Health 19 (2022), https://doi.org/10.3390/ijerph192416397.
[8] A.Pietro Tucci, S. Murgolo, C. De Ceglie, G. Mascolo, M. Carmagnani, A. Lucchini Huspek, M. Bestetti, S. Franz, Photoelectrocatalysis as an effective treatment for removing perfluoroalkyl substances from contaminated groundwaters: the real case of the veneto region (Italy), Water (Switz.) 17 (2025), https://doi.org/10.3390/w17182790.
[9] G.K. Longendyke, S. Katel, Y. Wang, PFAS fate and destruction mechanisms during thermal treatment: a comprehensive review, Environ. Sci. Process. Impacts 24 (2022) 196–208, https://doi.org/10.1039/d1em00465d.
[10] M.C. Collivignarelli, S. Bellazzi, F.M. Caccamo, S. Calatroni, C. Milanese, M. Baldi, A. Abbà, S. Sorlini, G. Bertanza, Removal of per- and polyfluoroalkyl substances by adsorption on innovative adsorbent materials, Sustainability 15 (2023), https://doi.org/10.3390/su151713056.

[11] K.H. Kang, C. Son, S. Bae, K. Chon, Y.M. Kim, Investigation of perfluorooctanoic acid and perfluorooctane sulfonate adsorption by Ca- and Fe-modified biochars: potential of Ca-modified biochar in real water matrices, Sep. Purif. Technol. 376 (2025), https://doi.org/10.1016/j.seppur.2025.133906.
[12] M. Hassan, J. Du, Y. Liu, R. Naidu, J. Zhang, M.A. Ahsan, F. Qi, Magnetic biochar for removal of perfluorooctane sulphonate (PFOS): interfacial interaction and adsorption mechanism, Environ. Technol. Innov. 28 (2022), https://doi.org/10.1016/j.eti.2022.102593.
[13] R. Zhang, Z. Ren, U. Bergmann, J.N. Uwayezu, I. Carabante, J. Kumpiene, T. Lejon, I. Levakov, G. Rytwo, T. Leiviskä, Removal of per- and polyfluoroalkyl substances (PFAS) from water using magnetic cetyltrimethylammonium bromide (CTAB)-modified pine bark, J. Environ. Chem. Eng. 12 (2024), https://doi.org/10.1016/j.jece.2024.114006.
[14] J. Han, C.E. Choong, M. Jang, J. Lee, S. Hyun, W.S. Lee, M. Kim, Causative mechanisms limiting the removal efficiency of short-chain per- and polyfluoroalkyl substances (PFAS) by activated carbon, Chemosphere 365 (2024), https://doi.org/10.1016/j.chemosphere.2024.143320.
[15] U. Kannan, M.K. Ravichandran, M. Monisha, S. Krishnasamy, Valliammai, P. Prabakar, D. Darshini, G. Sunantha, Short-chain PFAS: a global challenge - Environmental fate, health risks, and promising removal technologies, Results Chem. 20 (2026), https://doi.org/10.1016/j.rechem.2025.103000.
[16] G.S. Ha, M.G. Sim, B.H. Jeon, G. Baek, Bioremediation of perfluorooctanoic acid using microalgae with a transcriptomic approach, J. Hazard. Mater. 488 (2025), https://doi.org/10.1016/j.jhazmat.2025.137508.
[17] I. Kozyatnyk, V. Benavente, E. Weidemann, S. Jansson, Adsorption of organic contaminants of emerging concern using microalgae-derived hydrochars, Sci. Rep. 15 (2025), https://doi.org/10.1038/s41598-025-92717-y.
[18] M. Mantovani, E. Collina, M. Lasagni, F. Marazzi, V. Mezzanotte, Production of microalgal-based carbon encapsulated iron nanoparticles (ME-nFe) to remove heavy metals in wastewater, Environ. Sci. Pollut. Res. 30 (2023) 6730–6745, https://doi.org/10.1007/s11356-022-22506-x.
[19] F. Liu, J.J. Pignatello, R. Sun, X. Guan, F. Xiao, A comprehensive review of novel adsorbents for per- and polyfluoroalkyl substances in water, ACS ES T Water 4 (2024) 1191–1205, https://doi.org/10.1021/acsestwater.3c00569.
[20] V. Mezzanotte, F. Romagnoli, B. Ievina, M. Mantovani, M. Invernizzi, E. Ficara, E. Collina, LCA of zero valent iron nanoparticles encapsulated in algal biomass for polishing treated effluents, Environ. Clim. Technol. 26 (2022) 1196–1208, https://doi.org/10.2478/rtuect-2022-0090.
[21] M.I.A. Abdel Maksoud, R.A. Fahim, A.G. Bedir, A.I. Osman, M.M. Abouelela, G. S. El-Sayyad, M.A. Elkodous, A.S. Mahmoud, M.M. Rabee, A.H. Al-Muhtaseb, D. W. Rooney, Engineered magnetic oxides nanoparticles as efficient sorbents for wastewater remediation: a review, Environ. Chem. Lett. 20 (2022) 519–562, https://doi.org/10.1007/s10311-021-01351-3.
[22] A.M. Díaz, R. Forján, J.R. Gallego, L. Benavente-Hidalgo, J.M. Menéndez-Aguado, D. Baragaño, Nanoscale zero-valent iron mitigates arsenic mobilization and accumulation in Sinapis alba grown on a metal(loid)-polluted soil treated with a dunite mining waste-compost amendment, Plant Soil 497 (2024) 241–255, https://doi.org/10.1007/s11104-023-05879-x.
[23] E. Passalacqua, R. Correcher, M. Mantovani, E. Collina, A. Fullana, Use of carbon-encapsulated zero-valent iron nanoparticles from waste biomass to hydrogen sulphide wet removal, Waste Manag. Res. 43 (2025) 684–696, https://doi.org/10.1177/0734242X241273800.
[24] M. Sörengård, E. Östblom, S. Köhler, L. Ahrens, Adsorption behavior of per- And polyfluoralkyl substances (PFASs) to 44 inorganic and organic sorbents and use of dyes as proxies for PFAS sorption, J. Environ. Chem. Eng. 8 (2020), https://doi.org/10.1016/j.jece.2020.103744.
[25] M. Mantovani, S. Rossi, E. Ficara, E. Collina, F. Marazzi, M. Lasagni, V. Mezzanotte, Removal of pharmaceutical compounds from the liquid phase of anaerobic sludge in a pilot-scale high-rate algae-bacteria pond, Sci. Total Environ. 908 (2024), https://doi.org/10.1016/j.scitotenv.2023.167881.
[26] S. Rossi, M. Mantovani, F. Marazzi, V. Mezzanotte, E. Ficara, Long-term outdoor operation of microalgae-based digestate treatment: impact of external drivers on process performances and techno-economic assessment, Bioresour. Technol. 427 (2025), https://doi.org/10.1016/j.biortech.2025.132406.
[27] M. Mantovani, E. Collina, E. Passalacqua, M. Lasagni, V. Mezzanotte, Microalgal-based carbon encapsulated iron nanoparticles for the removal of pharmaceutical compounds from wastewater, J. Environ. Manag. 368 (2024), https://doi.org/10.1016/j.jenvman.2024.122171.
[28] A. Bhattarai, M. Khanal, D. Rai, R. Khanal, Determination of point zero charge (PZC) of homemade charcoals of Shorea robusta (Sakhuwa) and Pinus Roxburghii (Salla), Int. J. Eng. Res. Technol. (IJERT) 41 (2020), https://doi.org/10.17577/IJERTV9IS100046.
[29] U.S. Environmental Protection Agency, Method 1633: Analysis of Per- and Polyfluoroalkyl Substances (PFAS) in Aqueous, Solid, Biosolids, and Tissue Samples by LC-MS/MS, 2024.
[30] F. Fernandes, M. Freitas, C. Pinho, A.I. Oliveira, C. Delerue-Matos, C. Grosso, Upcycling coffee waste into sustainable nano zerovalent iron for environmental contaminant remediation: characterization, applicability and cytotoxicity, Nanomaterials 15 (2025), https://doi.org/10.3390/nano15231788.
[31] D. Mahl, J. Diendorf, W. Meyer-Zaika, M. Epple, Possibilities and limitations of different analytical methods for the size determination of a bimodal dispersion of metallic nanoparticles, Colloids Surf. A Physicochem. Eng. Asp. 377 (2011) 386–392, https://doi.org/10.1016/j.colsurfa.2011.01.031.
[32] I. Kozyatnyk, V. Benavente, E. Weidemann, F.G. Gentili, S. Jansson, Influence of hydrothermal carbonization conditions on the porosity, functionality, and sorption properties of microalgae hydrochars, Sci. Rep. 13 (2023), https://doi.org/10.1038/s41598-023-35331-0.
[33] K.J. Nakarmi, E. Daneshvar, G. Eshaq, L. Puro, A. Maiti, P.V. Nidheesh, H. Wang, A. Bhatnagar, Synthesis of biochar from iron-free and iron-containing microalgal biomass for the removal of pharmaceuticals from water, Environ. Res. 214 (2022), https://doi.org/10.1016/j.envres.2022.114041.
[34] T. Wang, Y. Zhai, Y. Zhu, C. Li, G. Zeng, A review of the hydrothermal carbonization of biomass waste for hydrochar formation: process conditions, fundamentals, and physicochemical properties, Renew. Sustain. Energy Rev. 90 (2018) 223–247, https://doi.org/10.1016/j.rser.2018.03.071.
[35] B. Calderon, F. Smith, I. Aracil, A. Fullana, Green synthesis of thin shell carbon-encapsulated iron nanoparticles via hydrothermal carbonization, ACS Sustain. Chem. Eng. 6 (2018) 7995–8002, https://doi.org/10.1021/acssuschemeng.8b01416.
[36] G. Binda, D. Spanu, R. Bettinetti, L. Magagnin, A. Pozzi, C. Dossi, Comprehensive comparison of microalgae-derived biochar from different feedstocks: a prospective study for future environmental applications, Algal Res. 52 (2020), https://doi.org/10.1016/j.algal.2020.102103.
[37] V.O. Shikuku, R. Zanella, C.O. Kowenje, F.F. Donato, N.M.G. Bandeira, O. D. Prestes, Single and binary adsorption of sulfonamide antibiotics onto iron-modified clay: linear and nonlinear isotherms, kinetics, thermodynamics, and mechanistic studies, Appl. Water Sci. 8 (2018), https://doi.org/10.1007/s13201-018-0825-4.
[38] J.H. Park, J.J. Wang, Y. Meng, Z. Wei, R.D. DeLaune, D.C. Seo, Adsorption/desorption behavior of cationic and anionic dyes by biochars prepared at normal and high pyrolysis temperatures, Colloids Surf. A Physicochem. Eng. Asp. 572 (2019) 274–282, https://doi.org/10.1016/j.colsurfa.2019.04.029.
[39] H. Son, T. Kim, H.S. Yoom, D. Zhao, B. An, The adsorption selectivity of short and long per-and polyfluoroalkyl substances (Pfass) from surface water using powder-activated carbon, Water 12 (2020), https://doi.org/10.3390/w12113287.
[40] X. Lei, Q. Lian, X. Zhang, T.K. Karsili, W. Holmes, Y. Chen, M.E. Zappi, D.D. Gang, A review of PFAS adsorption from aqueous solutions: current approaches, engineering applications, challenges, and opportunities, Environ. Pollut. 321 (2023), https://doi.org/10.1016/j.envpol.2023.121138.
[41] P.M. Rodrigo, C. Navarathna, M.T.H. Pham, S.J. McClain, S. Stokes, X. Zhang, F. Perez, S.R. Gunatilake, A.G. Karunanayake, R. Anderson, R.V.K.G. Thirumalai, D. Mohan, C.U. Pittman, T.E. Mlsna, Batch and fixed bed sorption of low to moderate concentrations of aqueous per- and poly-fluoroalkyl substances (PFAS) on Douglas fir biochar and its Fe3O4 hybrids, Chemosphere 308 (2022), https://doi.org/10.1016/j.chemosphere.2022.136155.
[42] M. Vakili, G. Cagnetta, S. Deng, W. Wang, Z. Gholami, F. Gholami, W. Dastyar, A. Mojiri, L. Blaney, Regeneration of exhausted adsorbents after PFAS adsorption: a critical review, J. Hazard. Mater. 471 (2024), https://doi.org/10.1016/j.jhazmat.2024.134429.
[43] W. Wang, A. Maimaiti, H. Shi, R. Wu, R. Wang, Z. Li, D. Qi, G. Yu, S. Deng, Adsorption behavior and mechanism of emerging perfluoro-2-propoxypropanoic acid (GenX) on activated carbons and resins, Chem. Eng. J. 364 (2019) 132–138, https://doi.org/10.1016/j.cej.2019.01.153.
[44] B.O. Fagbayigbo, B.O. Opeolu, O.S. Fatoki, Adsorption of perfluorooctanoic acid (PFOA) and perfluorooctane sulfonate (PFOS) from water using leaf biomass (Vitis vinifera) in a fixed-bed column study, J. Environ. Health Sci. Eng. 18 (2020) 221–233, https://doi.org/10.1007/s40201-020-00456-1.